JACS
JOURNAL OF THE AMERICAN CHEMICAL SOCIETY

Article

pubs.acs.org/JACS

Mechanism of H_2 Production by Models for the [NiFe]-Hydrogenases: Role of Reduced Hydrides

Olbelina A. Ulloa,[†] Mioy T. Huynh,[†] Casseday P. Richers,[†] Jeffery A. Bertke, Mark J. Nilges, Sharon Hammes-Schiffer,* and Thomas B. Rauchfuss*

Department of Chemistry, University of Illinois at Urbana-Champaign, Urbana, Illinois 61801, United States

Supporting Information

ABSTRACT: The intermediacy of a reduced nickel−iron hydride in hydrogen evolution catalyzed by Ni−Fe complexes was verified experimentally and computationally. In addition to catalyzing hydrogen evolution, the highly basic and bulky (dppv)Ni(μ-pdt)Fe(CO)(dppv) ([**1**]^0; dppv = *cis*-$C_2H_2(PPh_2)_2$) and its hydride derivatives have yielded to detailed characterization in terms of spectroscopy, bonding, and reactivity. The protonation of [**1**]^0 initially produces *unsym*-[H**1**]$^+$, which converts by a first-order pathway to *sym*-[H**1**]$^+$. These species have C_1 (unsym) and C_s (sym) symmetries, respectively, depending on the stereochemistry of the octahedral Fe site. Both experimental and computational studies show that [H**1**]$^+$ protonates at sulfur. The $S = 1/2$ hydride [H**1**]^0 was generated by reduction of [H**1**]$^+$ with Cp^*_2Co. Density functional theory (DFT) calculations indicate that [H**1**]^0 is best described as a Ni(I)−Fe(II) derivative with significant spin density on Ni and some delocalization on S and Fe. EPR spectroscopy reveals both kinetic and thermodynamic isomers of [H**1**]^0. Whereas [H**1**]$^+$ does not evolve H_2 upon protonation, treatment of [H**1**]^0 with acids gives H_2. The redox state of the "remote" metal (Ni) modulates the hydridic character of the Fe(II)−H center. As supported by DFT calculations, H_2 evolution proceeds either directly from [H**1**]^0 and external acid or from protonation of the Fe−H bond in [H**1**]^0 to give a labile dihydrogen complex. Stoichiometric tests indicate that protonation-induced hydrogen evolution from [H**1**]^0 initially produces [**1**]$^+$, which is reduced by [H**1**]^0. Our results reconcile the required reductive activation of a metal hydride and the resistance of metal hydrides toward reduction. This dichotomy is resolved by reduction of the remote (non-hydride) metal of the bimetallic unit.

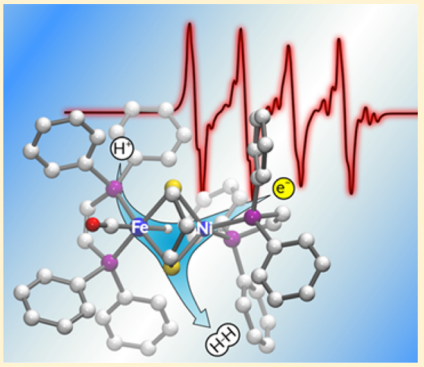

INTRODUCTION

The crystallographic characterization of the active sites of [NiFe]- and [FeFe]-hydrogenases (H_2ases) sparked the synthesis and study of many low molecular weight models. These models replicate some aspects of the biological reactions,[1] shedding light on how these enzymes operate and perhaps opening avenues for bioinspired if not biomimetic reactivity of interest in the energy sector.

Mechanistic attention is particularly focused on hydride-containing models since hydride is the substrate in both H_2 oxidation and proton reduction. Only a small number of hydride-containing models for the [NiFe]-enzymes have been designed.[2−4] A versatile family of models are of the type [(diphosphine)Ni(μ-pdt)(μ-H)Fe(CO)$_x$(PR$_3$)$_x$]$^+$ (pdt^{2-} = $S_2C_3H_6^{2-}$). In the case of the Fe(CO)$_3$ and Fe(CO)$_2$(PR$_3$) derivatives, the Ni−Fe hydrides are notable because they catalyze proton reduction,[2,3,5,6] as well as, in one case,[7] hydrogen oxidation.[8]

Hydrogen evolution catalyzed both by the enzymes and by the models operates by the intermediacy of Ni(II)−H−Fe(II) species.[9−11] In the enzyme, this species, the Ni−R state, releases H_2 via protonolysis to give an unsaturated Ni(II)−Fe(II) species (Ni−SI$_a$) (Scheme 1). The intimate details of H_2 release in the enzyme remain an area of active investigation,[12]

Scheme 1. Active Site States of [NiFe]-Hydrogenases[a]

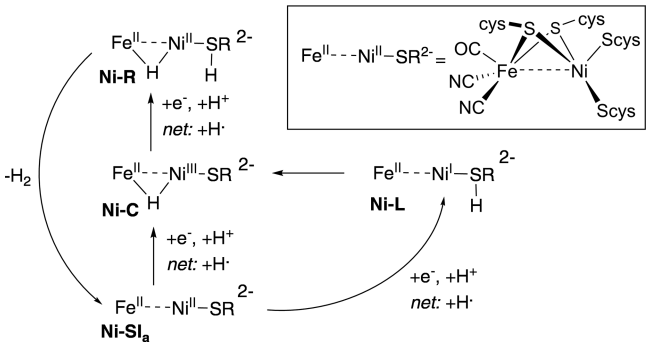

[a]Only unidirectional conversions are shown for simplicity.

one complicating aspect being the protonation state of the terminal thiolate cofactors. The Ni(II)−H−Fe(II) models do not release H_2 upon treatment with proton donors. Instead, hydrogen evolution occurs only upon reduction.[3,5,13,14] A similar pattern is often observed with Fe(II)−H−Fe(II)

Received: May 3, 2016
Published: June 21, 2016

DOI: 10.1021/jacs.6b04579
J. Am. Chem. Soc. 2016, 138, 9234−9245

Scheme 2. Synthesis of [(dppv)Ni(μ-pdt)Fe(CO)(dppv)]^0 ([1]^0) and Its Hydride Derivatives[a]

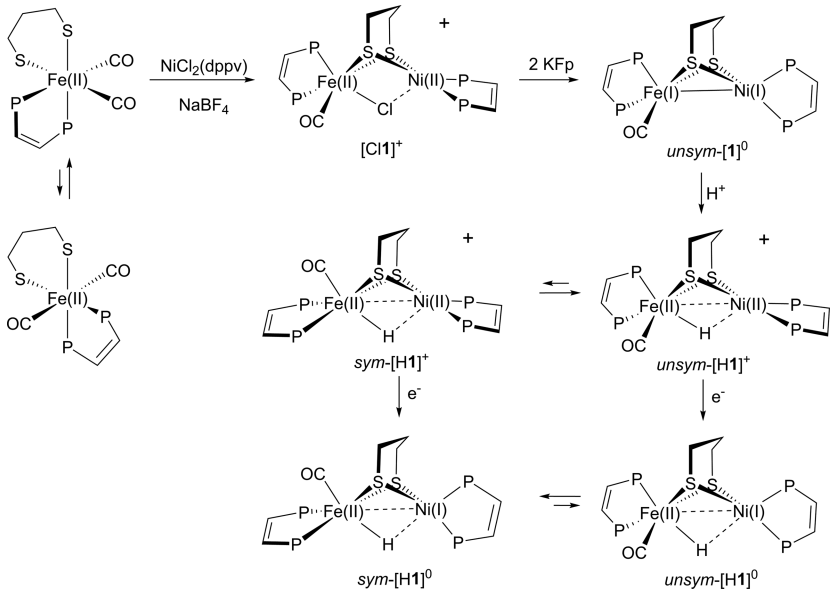

[a]Ph−P substituents omitted for clarity.

(bridging hydride[14]) and Fe(II)−Fe(II)−H (terminal hydride[15]) complexes, which also release H_2 only upon reduction.[16] For the [FeFe]-hydrogenase models, the electron-transfer-induced (ET-induced) protonation of an Fe(II)−Fe(II)−H species is explained by the involvement of a transient H_{sred} state featuring an appended [4Fe−4S]$^+$ subunit.[9]

Since hydrogen evolution from Ni−H−Fe complexes commences upon reduction, reduced Ni−H−Fe complexes represent important targets for characterization. Electrochemical reduction of the [(diphos)Ni(μ-pdt)(μ-H)Fe(CO)$_x$(PR$_3$)$_{3-x}$]$^+$ species leads to unstable products, however, probably owing to bimolecular degradation pathways.[3] Such bimolecular processes should be suppressed in sterically bulky Ni−Fe hydrides. For these reasons, our attention turned to [(dppv)Ni(μ-pdt)(μ-H)Fe(CO)(dppv)]^z, a new family of [NiFe]-hydrogenase models related to the [(dppv)(CO)Fe(μ-pdt)(μ-H)Fe(CO)(dppv)]^z platform that has illuminated aspects of hydrogenase chemistry.[14,17] The dppv ligand confers stability to these models and minimizes side reactions that can plague more flexible chelating diphosphines.[18,19]

Starting with the preparation and protonation of [(dppv)Ni(μ-pdt)(μ-H)Fe(CO)(dppv)]^0 ([**1**]^0), in this paper we describe previously unseen insights related to hydrogen evolution catalysis. Of particular interest is the observation of the reduced hydride, which is the species that is protonated, thereby liberating H_2. Our results reconcile the required reductive activation of a metal hydride and the resistance of metal hydrides toward reduction.[20] This dichotomy is shown to be resolved when ET occurs at the remote (non-hydride) metal of the bimetallic unit.

RESULTS AND DISCUSSION

Following precedent for related reactions,[2] the synthesis of [**1**]^0 began with the reaction of Fe(pdt)(dppv)(CO)$_2$, NiCl$_2$(dppv), and NaBF$_4$ to give the Ni(II)−Fe(II) species [(dppv)Ni(μ-pdt)(μ-Cl)Fe(CO)(dppv)]BF$_4$ ([Cl**1**]BF$_4$). Although Fe(pdt)(CO)$_2$(dppv) consists of a 1:4 mixture of all-cis and trans isomers, the initially formed [Cl**1**]$^+$ consists only of the unsymmetrical (unsym) isomer wherein the dppv on Fe spans apical and basal coordination sites. Reduction of a THF solution of *unsym*-[Cl**1**]BF$_4$ with KFe(CO)$_2$Cp gave [**1**]^0 (Scheme 2).

At room temperature, the ^{31}P{^{1}H} NMR spectrum of [**1**]^0 in C$_6$D$_6$ solution is simple: signals assigned to the Fe(CO)(dppv) center appear as a triplet (δ 89.2), and those assigned to the Ni(dppv) center appear as two doublets (δ 74.2 and 46.2). These assignments are consistent with the ^{31}P{^{1}H} NMR spectrum of the ^{57}Fe derivative, which revealed broadening of the signal assigned to the Fe(CO)(dppv) center (Figure S19). The chemical shifts of the signals assigned to the Ni(dppv) group are similar to those for [(dppe)Ni(μ-pdt)Fe(CO)$_3$]^0 (δ 81 and 46, at −68 °C).[3] The Ni(dppe) center of [(dppe)Ni(μ-pdt)Fe(CO)$_3$]^0 is dynamic on the NMR time scale, such that only a single ^{31}P signal (δ 63.6) appears at 20 °C.[6] In contrast, two ^{31}P signals assigned to the Ni(dppv) site in [**1**]^0 are observed even up to 90 °C, indicating a barrier to rotation at Ni of >14 kcal/mol (Figure S23). Upon cooling a toluene solution of [**1**]^0 below −65 °C, four signals appear in the ^{31}P{^{1}H} NMR spectrum. This decoalescence reveals the full complexity of this chiral species.

Crystallographic analysis of [**1**]^0 confirms the unsymmetrical structure suggested by the NMR data (Figure 1). The Fe−Ni bond of 2.5261(4) Å is 0.06 Å longer than that for [(dppe)Ni(μ-pdt)Fe(CO)$_3$]^0 (2.466(6) Å),[19] an elongation attributed to steric interactions between the two bulky M(dppv) centers. The iron center of [**1**]^0 adopts a distorted octahedral geometry, viewing the Fe−Ni bond as a sixth ligand. The nickel center adopts a distorted trigonal bipyramidal geometry, viewing the Fe−Ni bond as a fifth ligand, in addition to two phosphines and two thiolates. The Fe$_1$−Ni$_1$−P$_2$ angle is 162.2°, and the dihedral angle is 80.94° for the S$_1$−Ni−S$_2$ and P$_1$−Ni−P$_2$ planes. For comparison, the corresponding values for [(dppe)Ni(μ-pdt)Fe(CO)$_3$]^0 are 169.8° and 84.9°.[19] The Ni−P distances are comparable to those in Ni(dppv)$_2$ (2.1414(6)−2.1586(6) Å) as well as [(dppe)Ni(μ-pdt)Fe(CO)$_3$]^0 (2.159−2.146 Å).[19]

DOI: 10.1021/jacs.6b04579
J. Am. Chem. Soc. 2016, 138, 9234−9245

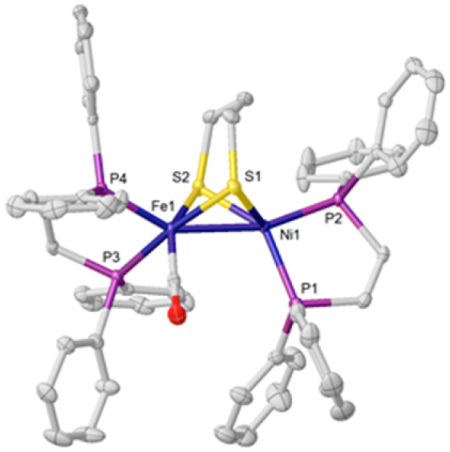

Figure 1. Molecular structure of the non-hydrogen atoms of $[\mathbf{1}]^0$ showing 50% probability ellipsoids.

Density Functional Theory (DFT)-Optimized Structure of $[\mathbf{1}]^0$. The DFT-optimized structure of $[\mathbf{1}]^0$ is in good agreement with the crystal structure. Similar to related dithiolate compounds,[6,19] $[\mathbf{1}]^0$ also contains a Ni–Fe σ-bond that can be localized using either the natural bond orbital (NBO)[21] or the Pipek–Mezey criterion (Figure S61).[22]

The ^{31}P NMR resonance at δ 89 is assigned to the Fe(CO)(dppv) center. This signal decoalesces at low temperatures in toluene, indicating a rotational barrier of ~9 kcal/mol, in good agreement with the DFT-calculated free energy barrier of $\Delta G^{\ddagger}$ = 9.55 kcal/mol in toluene. Interchange of the P–Fe sites could conceivably occur via an intermediate wherein the dppv occupies dibasal sites (i.e., sites that are trans to the dithiolate) and the CO ligand occupies the apical site trans to nickel. According to our calculations, the formation of this dibasal intermediate is thermodynamically accessible (ΔG° = 5.26 kcal/mol) but is subject to a high free energy barrier of 27 kcal/mol in toluene. A lower free energy pathway is shown in Scheme 3 with a transition state (TS) in which the dppv ligand occupies sites cis to the dithiolate. In the TS structure, the Ni–Fe bond remains ~2.52 Å. A similar pathway has been invoked for $Fe_2(\mu$-pdt)$(CO)_4$(diphos) and related complexes.[23,24]

The calculations do not reveal a minimum with a square planar Ni center. In contrast, previous calculations on $[(dppe)Ni(\mu$-pdt)$Fe(CO)_3]^0$ showed that the valence isomers, with either square planar Ni(II) or tetrahedral Ni(I) centers, are nearly isoergic. Formation of square planar Ni(II) requires an intramolecular electron transfer to convert Fe(I) to Fe(0). The $[(dppe)Ni(\mu$-pdt)$Fe(CO)_3]^{+/0}$ couple (−0.59 V) is ~300 mV milder than the $[\mathbf{1}]^{+/0}$ couple, indicating the greater reluctance for the $(RS)_2Fe(CO)$(dppv) vs $(RS)_2Fe(CO)_3$ site to undergo reduction from Fe(I) to Fe(0) in $[\mathbf{1}]^0$.[6]

The IR spectrum of $[\mathbf{1}]^0$ in THF solution shows a dominant ν_{CO} band at 1897 cm^{-1} with a shoulder at ~1912 cm^{-1}. These signals probably arise from two conformers ("flippamers"), resulting from the relative orientation of the propanedithiolate backbone. DFT predicts ν_{CO} values of 1905 and 1908 cm^{-1} for the two flippamers of the unsym isomer.

Redox of $[\mathbf{1}]^0$. Cyclic voltammetry (CV) studies on a 1,2-$C_6H_4F_2$ solution of $[\mathbf{1}]^0$ revealed a single redox couple assigned to $[\mathbf{1}]^{+/0}$ at −1.13 V vs $Fc^{0/+}$. The couple is quasi-reversible on the basis of the current ratio, $i_{pa}/i_{pc} \approx 1.16$, and a fairly linear dependence of i vs (scan rate)$^{1/2}$ (Figures S47, S48). Reflecting the highly reactive nature of $[\mathbf{1}]^+$, the CV of a PhCN solution was very different, involving two oxidation and two reduction processes. The latter processes are almost certainly the result of solvent coordination.

DFT Characterization of $[\mathbf{1}]^+$. Using DFT, two valence isomers were characterized for $[\mathbf{1}]^+$. These two isomers differ in oxidation states for the two metals: Ni(I)Fe(II) vs Ni(II)Fe(I). The calculations indicate that these two species also differ with respect to the geometry at Ni (Figure 2). Moreover, the Fe–Ni bond is disrupted (2.91 Å) in the Ni(II)-Fe(I) valence isomer compared to the Ni(I)-Fe(II) valence isomer (2.52 Å). The sym isomer of $[\mathbf{1}]^+$ was also characterized using DFT, and is qualitatively similar to the unsym isomer presented here.

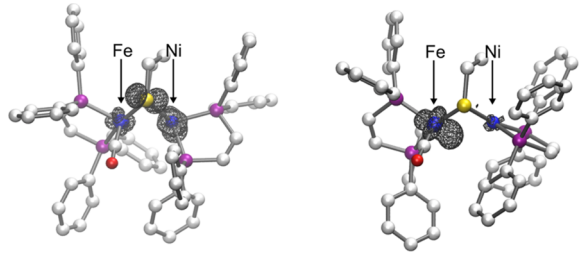

Figure 2. Spin density plots (isovalue 0.005) for the Ni(I)Fe(II) (left) and Ni(II)Fe(I) (right) valence isomers of *unsym*-$[\mathbf{1}]^+$.

The spin densities for these two valence isomers are given in Table 1. The calculated reaction free energy is small (ΔG° = −1.36 kcal/mol) for the isomerization from Ni(II)Fe(I) to Ni(I)Fe(II), and the calculated free energy barrier for this

Table 1. Calculated Spin Densities for the Valence Isomers of $[\mathbf{1}]^+$ [a]

valence isomer	ρ(Ni)	ρ(Fe)	ρ(2S)	$\rho(2P_{Ni})$[b]	$\rho(2P_{Fe})$[c]
Ni(II)Fe(I)	0.05	0.87	−0.02	0.01	0.05
	0.05	0.90	−0.02	0.01	0.05
Ni(I)Fe(II)	0.59	0.04	0.33	0.03	−0.02
	0.64	−0.05	0.32	0.05	0.00

[a]For each valence isomer, the first and second entries correspond to the unsym and sym isomers, respectively. [b]These values refer to the P atoms of the dppv ligand on the Ni center. [c]These values refer to the P atoms of the dppv ligand on the Fe center.

Scheme 3. DFT-Calculated Low-Energy Pathway for Degenerate Isomerization of $[\mathbf{1}]^0$ [a]

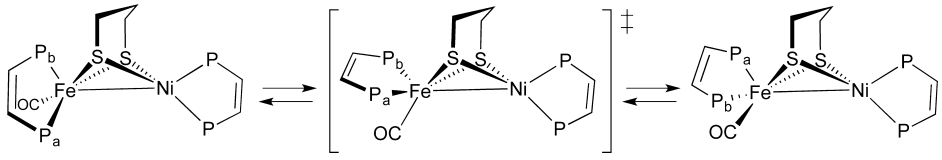

[a]Notice that the dibasal isomer is not an intermediate in this process (Ph–P groups omitted for clarity).

DOI: 10.1021/jacs.6b04579
J. Am. Chem. Soc. 2016, 138, 9234–9245

Scheme 4. Variable-Temperature NMR Measurements Establish That the Ni(II) Site Is Nonrigid in *unsym*-[H1]$^+$ [a]

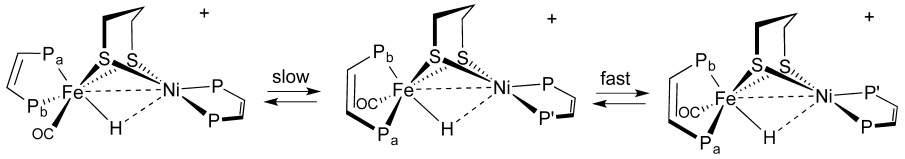

[a]Ph−P groups were omitted for clarity. Note that the interconversion of P and P′ at the Ni center in the fast step indicates rotation about this center.

isomerization is also relatively low ($\Delta G^{\ddagger}$ = 2.75 kcal/mol). Thus, the calculations indicate that both isomers could be thermally accessible at room temperature but do not allow for the identification of a kinetic or thermodynamic preference. The calculated ν_{CO} values are 1948 and 1913 cm^{-1} for the Ni(I)Fe(II) and Ni(II)Fe(I) valence isomers, respectively.

Protonation of [1]^0. Protonation of [**1**]^0 with HOTf or $H(OEt_2)_2BAr^F{}_4$ afforded a single unsymmetrical isomer of [H**1**]$^+$ (Scheme 2). Three $^{31}P\{^1H\}$ NMR signals (intensities 1:1:2) for *unsym*-[H**1**]$^+$ appear at δ 87.8, 80.6, and 72.8, respectively. The lower field signals are assigned to the Fe(dppv) group, and the signal at δ 72.8 is assigned to the Ni(dppv) group. Upon cooling the toluene solution of [H**1**]$^+$ to −40 °C, the Ni(dppv) signal decoalesces into two broad singlets (Figure S33). These observations are consistent with the Fe center being more rigid than the Ni site (Scheme 4).

Over the course of a few hours in MeCN solution at 25 °C, *unsym*-[H**1**]$^+$ partially converts to *sym*-[H**1**]$^+$ (Scheme 2). The conversion follows first-order kinetics with a rate of 5.2 × 10^{-5} s^{-1}. On the basis of transition-state theory, this rate for conversion of *unsym*-[H**1**]$^+$ to *sym*-[H**1**]$^+$ corresponds to $\Delta G^{\ddagger}$ ≈ 23 kcal/mol. The DFT-calculated free energy barrier for this isomerization is 24 kcal/mol. The symmetrical isomer gives rise to two singlets in the $^{31}P\{^1H\}$ NMR spectrum. Consistent with its high symmetry, *sym*-[H**1**]$^+$ exhibits a $^{31}P\{^1H\}$ NMR spectrum that does not change over the range +35 to −40 °C. At equilibrium, the sym:unsym ratio is 1:5 and 1:8 in MeCN and CH_2Cl_2 solutions, respectively.

Crystallographic and DFT Analysis of the Ni(II)−H−Fe(II) Complex. The salt *unsym*-[H**1**]$BAr^F{}_4$ was characterized crystallographically. It features an octahedral iron center and an approximately square pyramidal nickel center (Figure 3). The Fe center adopts the unsym geometry, which is the predominant isomer in solution.

The structures of both the sym and unsym isomers of [H**1**]$^+$ were optimized using DFT, and the unsym isomer was found to be 2.35 kcal/mol lower in free energy than the sym isomer. The optimized unsym structure agrees well with the crystallographic result, as shown by the selected bond lengths and angles provided in Table 2. Consistent with the crystal structure of *unsym*-[H**1**]$^+$, the optimized structures of *sym*-[H**1**]$^+$ and *unsym*-[H**1**]$^+$ both feature asymmetrically bound hydrides, with the hydride closer to Fe than to Ni. The DFT-optimized structure of *sym*-[H**1**]$^+$ is provided in the Supporting Information (Table S31). Moreover, consistent with previous DFT calculations on NiFe models,[24] the CO stretching frequencies (ν_{CO}) for the optimized structures agree well with the experimental IR data (Table 3). The values 1946 and 1957 cm^{-1} were calculated for the sym and unsym isomers, respectively. These values shift by 1−4 cm^{-1}, depending on the conformation of the pdt backbone (Table S15).

Acid−Base Properties of [H1]$^+$. The pK_a of [H**1**]$^+$ was determined by treating [**1**]^0 with varying amounts of acetic acid

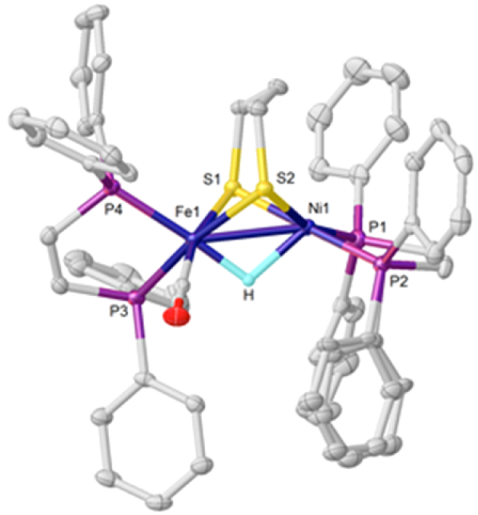

Figure 3. Molecular structure of the cation in [H**1**]$BAr^F{}_4$ with 50% probability thermal ellipsoids. This structure corresponds to the unsym isomer. Hydrogen atoms that were not refined, the counterion, and solvent molecules have been omitted for clarity.

(pK_a^{MeCN} = 21.56) to give mixtures of [**1**]^0 and *unsym*-[H**1**]$^+$. The $^{31}P\{^1H\}$ NMR signals for [**1**]^0 and *unsym*-[H**1**]$^+$ are distinct, consistent with slow proton exchange between the metal hydride and its conjugate base.[25,26] For these experiments, PhCN was used as the solvent under the assumption that pKa^{MeCN} ≈ pKa^{PhCN}.[27] In MeCN solution, HOAc and OAc^- tend to associate, as indicated by the homoconjugation constant of 3.21.[26] Our calculations corrected for this effect (Table S7). The pK_a of [H**1**]$^+$ is estimated to be 16.6 ± 0.04.[25] A pK_a of 17.7 for [H**1**]$^+$ was calculated by DFT relative to the reference pK_a for [(dppe)Ni(μ-pdt)(μ-H)Fe(CO)$_2$(PPh$_3$)]$^+$. As expected for a more electron-rich metal hydride, the pK_a of [H**1**]$^+$ is higher than that for related complexes substituted by only two or three phosphines. For example, pK_a^{PhCN} = 10.7 and 14.9 for [(dppe)Ni(μ-pdt)(μ-H)Fe(CO)$_3$]$^+$ and [(dppe)Ni(μ-pdt)(μ-H)Fe(CO)$_2$(PPh$_3$)]$^+$, respectively.[3] The DFT-calculated relative pK_a values for these species are also in good agreement with the experimental values and are provided in the Supporting Information (Table S18).

In CH_2Cl_2 solution, [H**1**]$^+$ is protonated by $[H(OEt_2)_2]$-$BAr^F{}_4$ to give a species denoted [H**1**H]$^{2+}$. The reaction is indicated by a color change from orange to red-brown. In the IR spectrum, ν_{CO} shifts from ∼1956 to 1994 cm^{-1} (Figure 4). The same protonation cannot be effected in THF, and addition of THF (100 μL) to a ∼9 mM solution of [H**1**H]$^{2+}$ in CH_2Cl_2 gave back [H**1**]$^+$, attesting to the highly acidic nature of the dication. The ^{31}P NMR spectrum of [H**1**H]$^{2+}$ shows four multiplets, indicating that the four phosphorus centers are nonequivalent, which indicates that (i) the compound is relatively rigid and (ii) protonation is regiospecific. In contrast, *sym*-[H**1**]$^+$ is dynamic on the ^{31}P NMR time scale owing to

DOI: 10.1021/jacs.6b04579
J. Am. Chem. Soc. 2016, 138, 9234−9245

Table 2. Selected Structural Metrics (Å, deg) for $[\mathbf{1}]^0$, *unsym*-$[\mathbf{H1}]^+$ (as the $BAr^F{}_4^-$ Salt), and *sym*-$[\mathbf{H1}]^0$

	unsym-$[\mathbf{1}]^0$		*unsym*-$[\mathbf{H1}]^+$		*sym*-$[\mathbf{H1}]^0$
	exptl	calcd[a]	exptl	calcd[a]	calcd[a]
Fe–Ni	2.5261(4)	2.523	2.6461(5)	2.686	2.691
Fe–H			1.56(3)	1.609	1.631
Ni–H			1.80(2)	1.812	1.808
$Ni–P_1$	2.1557(8)	2.186	2.1379(8)	2.187	2.254
$Ni–P_2$	2.1640(6)	2.184	2.1557(8)	2.210	2.200
$Fe–P_3$	2.2174(5)	2.203	2.2021(8)	2.277	2.278
$Fe–P_4$	2.1923(8)	2.256	2.2250(8)	2.257	2.241
$P_1–Ni–P_2/S_1–Ni–S_2$ dihedral angle[b] (deg)	80.94	79.19	15.97	17.56	104.78
$P_1–Ni–P_2$ bite angle (deg)	89.54	90.09	87.50	88.67	87.26
$P_3–Fe–P_4$ bite angle (deg)	86.27	87.08	86.43	87.21	87.17

[a]The omission of counterions in the calculations may introduce discrepancies between the crystal structure and DFT-optimized structure. [b]Dihedral refers to the angle between the planes formed by the groups of three atoms listed.

Table 3. Experimental and Calculated Values for ν_{CO} (cm^{-1})

	ν_{CO}(exptl)[a,b]	ν_{CO}(DFT)[c]
$[Cl\mathbf{1}]BF_4$	1946	n/a
$[\mathbf{1}]^0$	1912 (sh),[d] 1897	1905
$[\mathbf{H1}]^+$	1953	1946 (sym)
	1960 (sh)[d]	1957 (unsym)
$[\mathbf{H1H}]^{2+}$	1994 (unsym)	1980 (unsym)
$[\mathbf{H1}]^0$	1920	1922

[a]Experiments performed in THF solution unless otherwise noted. [b]The counterions for salts are $BAr^F{}_4^-$ except in the cases of $[\mathbf{1}]PF_6$ and $[Cl\mathbf{1}]BF_4$. [c]The central CH_2 of the pdt^{2-} is oriented toward the Ni center in all cases. The ν_{CO} values for the structures with the central CH_2 of the pdt^{2-} oriented toward the Fe center are provided in the Supporting Information (Table S15). These values shift by 1–4 cm^{-1} depending on the pdt^{2-} conformation. [d]sh = shoulder.

rotation of the square planar Ni center. Solutions of $[\mathbf{H1H}]^{2+}$ in CD_2Cl_2 are stable for hours. The ^1H NMR spectrum of $[\mathbf{H1H}]^{2+}$ shows a single hydride signal at δ −13.1. This hydride signal is shifted upfield of $[\mathbf{H1}]^+$ by 7.2 ppm and integrates to 1H.

The structure of $[\mathbf{H1H}]^{2+}$ and its interaction with OEt_2 were examined by DFT. The inclusion of neutral OEt_2 in these calculations is relevant because the acid was $[H(OEt_2)_2]^+$. The calculations show that H^+ and $H(OEt_2)^+$ regiospecifically protonate one of the two diastereotopic thiolate sulfur centers. Protonation by H^+ breaks the Ni–S bond trans to the basal Fe–P, as indicated by elongation of the Ni–S distance from 2.25 to 3.66 Å. However, the Ni–S bond is not disrupted when the ether is included in the optimization of $[\mathbf{H1H}]^{2+}$ (Figure 5). A possible explanation for the observation that ether stabilizes the bidentate over the monodentate structure is that the hydrogen bonding of ether to the SH group increases the basicity of the sulfur, allowing it to donate electrons more easily to the positively charged Ni center. The DFT-calculated values for ν_{CO} for the protonated species are 1980 and 1981 cm^{-1} for the structures with and without OEt_2, respectively. The *S*-protonation of bridging dithiolates in diiron complexes by HBF_4 and HOTf, as well as the disruption of the metal–sulfur bond, has been observed previously.[28]

Redox Experiments on Hydrides. Cyclic voltammetry (CV) studies on $[\mathbf{H1}]^+$ revealed that the hydride $[\mathbf{H1}]^+$ reversibly reduces to $[\mathbf{H1}]^0$ (Figure 6) at −1.48 V vs $Fc^{0/+}$ in MeCN (Table 4). In fact, all complexes of the type $[(diphosphine)Ni^{II}(\mu\text{-pdt})(\mu\text{-H})Fe^{II}(CO)_{3-x}(PR_3)_x]^+$ reduce

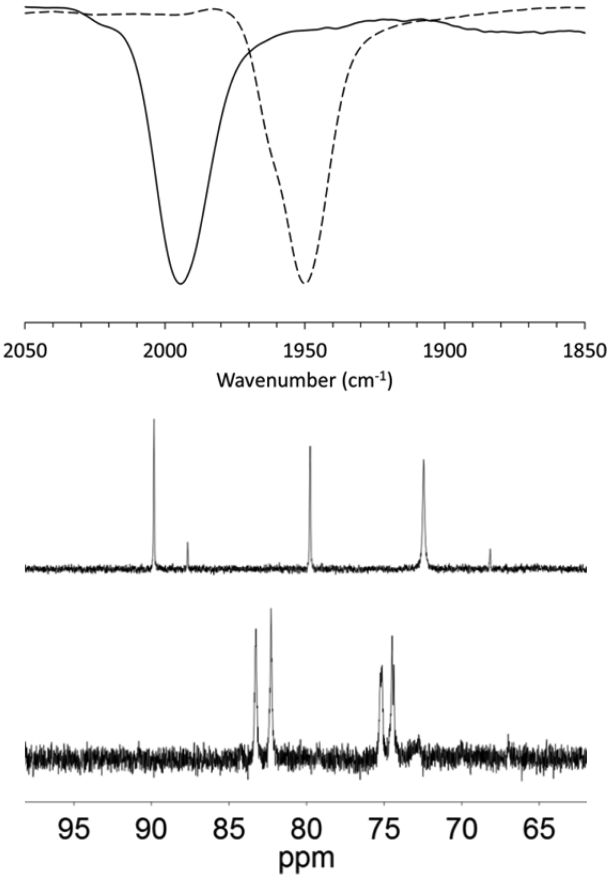

Figure 4. Spectroscopic changes induced by protonation of $[\mathbf{H1}]^+$ at room temperature. Top: FT-IR spectra of $[\mathbf{H1}]^+$ (dashed) and $[\mathbf{H1H}]^{2+}$ (solid) in CH_2Cl_2. Bottom: ^{31}P NMR spectra of a thermally equilibrated spectrum of $[\mathbf{H1}]^+$ (top) and a freshly prepared solution of $[\mathbf{H1H}]^{2+}$ (bottom) in CH_2Cl_2 (weak signals at δ 88 and 68 in the upper spectrum correspond to the sym isomer).

at similar potentials regardless of the substitution at Fe, consistent with a Ni-centered reduction.[3] The main difference among their redox behaviors is the reversibility, which improves with steric bulk such that the current ratio, i_{pa}/i_{pc}, for the $[\mathbf{H1}]^{+/0}$ couple is 0.94 at 100 mV/s in MeCN (Table S3). The DFT-calculated potential for the $[\mathbf{H1}]^{+/0}$ couple agrees with the experimental value (Table 4).

Hydrogen Evolution Catalysis. The hydrides are catalysts for hydrogen evolution. In the presence of TsOH (pK_a^{MeCN} =

DOI: 10.1021/jacs.6b04579
J. Am. Chem. Soc. 2016, 138, 9234–9245

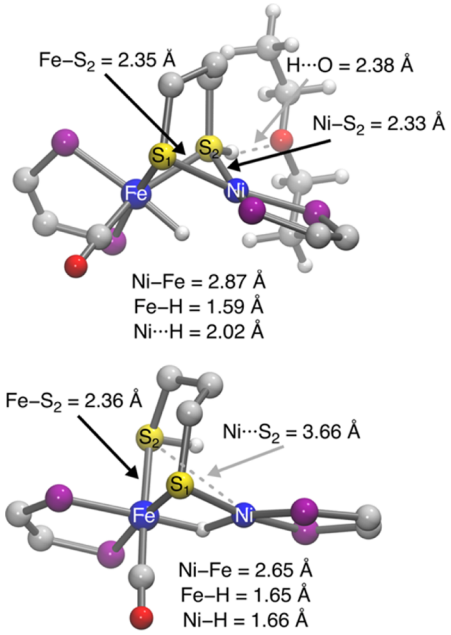

Figure 5. DFT-calculated structure of $[H1H]^{2+}$ with (top) and without (bottom) the interaction of the acidic proton with neutral OEt_2. Phenyl groups and most hydrogens were omitted for clarity. Another minimum energy structure was obtained by starting with the lower monodentate structure and adding an ether within hydrogen-bonding distance of S_2H; this optimized structure retained the monodentate character and was ~8 kcal/mol higher in free energy than the upper bidentate structure.

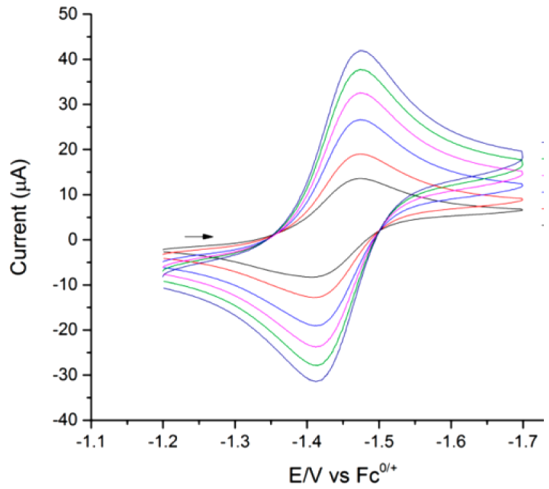

Figure 6. Cyclic voltammogram of $[H1]^{+/0}$ at scan rates of 50–500 mV/s. Conditions: 0.1 M $[Bu_4N]PF_6$ in MeCN, 1 mM [H1]OTf, glassy carbon working electrode, Ag/AgCl reference electrode, and Pt wire counter electrode.

8.7), CF_3CO_2H (pK_a^{MeCN} = 12.7),[29] and $ClCH_2CO_2H$ (pK_a^{MeCN} = 15.3), voltammograms of $[H1]^+$ in CH_2Cl_2 an MeCN solution showed increased currents at potentials corresponding to the reductive wave near −1.4 V, clear evidence for catalysis. The rate of hydrogen evolution exhibits a "plateau catalytic current" at high $[H^+]$ and scan rates. The rates were estimated by the foot-of-the-wave method, focusing on the slope of the i–V response at the onset of a catalytic current.[30] Analysis of the data for reduction of toluenesulfonic acid in MeCN solution yields a turnover frequency (TOF) of

Table 4. Current Ratios (i_{pa}/i_{pc}) and Observed and Calculated Redox Potentials (V vs $Fc^{0/+}$) for Ni–H–Fe Complexes[a]

redox couple	$E_{1/2}$(exptl)	i_{pa}/i_{pc}	$E_{1/2}$(DFT)
$[(dppe)Ni(\mu\text{-}pdt)(\mu\text{-}H)Fe(CO)_2(P(OPh)_3)]^{+/0}$	−1.44[3]	0.93[3]	−1.44[b]
$[(dppe)Ni(\mu\text{-}pdt)(\mu\text{-}H)Fe(CO)_2(PPh_3)]^{+/0}$	−1.49[3]	0.06[3]	−1.53
$[(dppe)Ni(\mu\text{-}pdt)(\mu\text{-}H)Fe(CO)_3]^{+/0}$	−1.29[3]	0.26[3]	−1.37
$[(dppv)Ni(\mu\text{-}pdt)(\mu\text{-}H)Fe(CO)(dppv)]^{+/0}$ ($[H1]^{+/0}$)	−1.48	0.94	−1.45

[a]Conditions: 1 mM complex in MeCN, 0.1 M $[NBu_4]BF_4$ electrolyte, glassy carbon electrode, 100 mV/s scan rate. [b]This couple was used as the reference for all other calculated potentials, so the experimental and calculated values agree by construction. Because the experimental reference is $E_{1/2}$, the calculated potentials are also assumed to be $E_{1/2}$.

480 s^{-1} (Figure S42). The production of hydrogen was confirmed by gas chromatographic analysis of the headspace gas after bulk electrolysis. Electrolysis for 1 h at −1.8 V vs $Fc^{0/+}$ afforded a faradaic yield of 93% H_2 (Figure S43).

Reduced Hydride [(dppv)Ni(μ-pdt)(μ-H)Fe(CO)(dppv)]^0, [H1]^0. Characterization of the reduced hydride was pursued to gain insight into the mechanism for hydrogen evolution. As indicated above, the $[H1]^{+/0}$ couple proceeds with good reversibility. Treatment of THF solutions of $[H1]^+$ with 1 equiv of $CoCp^*_2$ afforded a dark brown species with a single new ν_{CO} band, shifted by 25 cm^{-1} toward lower energy (Figure 7).

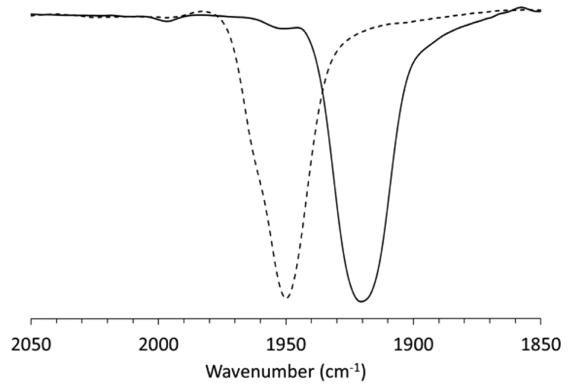

Figure 7. FT-IR spectra of THF solutions of $[H1]BAr^F_4$ (dashed line) and $[H1]^0$ (solid line).

The stability of THF solutions of $[H1]^0$ ranges from hours to days at room temperature, the rates apparently depending on the sample quality. Analysis of the headspace gas from a 50 mM solution of $[H1]^0$ that had been standing at 26 °C for 3.6 h revealed that approximately 0.35 equiv of H_2 (70% of theory, eq 1) was produced for every equivalent of $[H1]^0$ consumed. IR spectra in the ν_{CO} region showed isosbestic behavior (Figures S49 and S50). When the decay of $[H1]^0$ was followed by $^{31}P\{^1H\}$ NMR spectroscopy, $[1]^0$ was the exclusive product.

$$2[H1]^0 \rightarrow 2[1]^0 + H_2 \quad (1)$$

The EPR spectrum of freshly prepared $[H1]^0$ was simulated as three overlapping sets of signals with g_{iso} = 2.059, 2.056, and 2.030 (Figure 8). The ratio changes over the course of several minutes after the reduction (Figure S51), a process attributed to isomerization. The time dependence of the EPR spectrum is

DOI: 10.1021/jacs.6b04579
J. Am. Chem. Soc. 2016, 138, 9234–9245

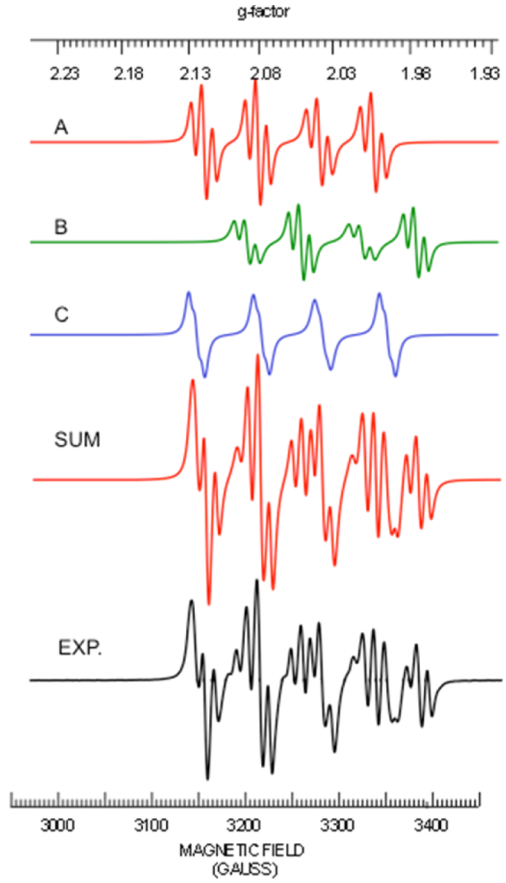

Figure 8. EPR spectrum of a THF solution of $[H1]^0$ freshly reduced at −77 °C (black), together with a simulated spectrum of the three components and their sum.

mirrored by IR measurements: a freshly reduced sample showed ν_{CO} at 1914 cm^{-1}, which shifted to 1920 cm^{-1} after several minutes (Figure S48). The rate of isomerization, with a half-life of 2 min, is about 1000× faster than the rates for interconversion of *sym*- and *unsym*-$[H1]^0$. The ratio of the three species is initially 1:1.2:1, respectively, reaching 1:0.1:0.1 upon equilibration (Figure 9). Each of these three species gives rise to a similar splitting pattern arising from $A \approx 360$ and 160 MHz and two smaller hyperfine splittings around 25 MHz (Table 5). The large hyperfine coupling constants are assigned to

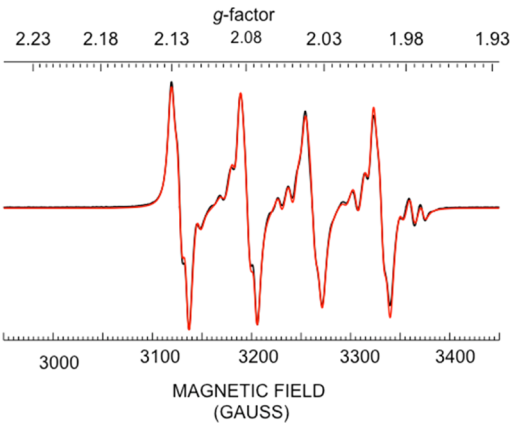

Figure 9. EPR spectrum of a THF solution of $[H1]^0$ equilibrated at 25 °C in red, together with a simulated spectrum in black.

Table 5. EPR Simulation Parameters for $[H1]^0$

species	*g* factor	$A(^{31}P)$ (MHz)
unsym-$[H1]^0$ (flippamer a)	2.059	355, 166, 34, 30
unsym-$[H1]^0$ (flippamer b)	2.030	348, 164, 33, 28
sym-$[H1]^0$	2.056	387, 199, 22, 14

interactions of the unpaired electron with the two ^{31}P(Ni) centers, while the two smaller coupling constants are assigned to interactions of the unpaired electron with the two ^{31}P(Fe) centers. Two of the three species are attributed to two flippamers of *unsym*-$[H1]^0$, while the third species is assigned as *sym*-$[H1]^0$. The observation of only one flippamer of *sym*-$[H1]^0$ is consistent with the unsymmetrical steric environment around the central CH_2 of the pdt^{2-} ligand. The EPR spectra of $[H1]^0$ and $[H1-^{57}Fe]^0$ were indistinguishable, consistent with the spin primarily localized on Ni (Figure S52). Coupling assignable to the hydride was not observed as indicated by the small difference between the experimental and simulated spectra.[16]

The changes in the EPR spectrum suggest that the kinetic product, enriched in the unsym isomer, isomerizes to the thermodynamic sym isomer. To independently verify this analysis, a thermally equilibrated MeCN solution of $[H1]^0$ was treated with 1 equiv of $FcBF_4$ to "freeze" the isomer ratio. The result, measured at 20 min at room temperature, was a 53:47 ratio of *unsym*-$[H1]^+$ to *sym*-$[H1]^+$. This isomer ratio is significantly enriched in the sym isomer relative to the thermodynamic ratio (85:15 favoring unsym).

DFT Characterization of $[H1]^0$. DFT calculations were also carried out on the reduced mixed-valence species to obtain further structural, energetic, and mechanistic insights. The calculations indicate that the Ni center changes from square planar to tetrahedral in the conversion of $[H1]^+$ to $[H1]^0$ (Scheme 2). This change in geometry is consistent with the description of the reduced complex $[H1]^0$ as Ni(I)Fe(II).[31] Structural metrics for *unsym*-$[H1]^0$ can be found in Table S13, and the optimized Cartesian coordinates for *sym*- and *unsym*-$[H1]^0$ can be found in Tables S36–S43. Although the geometry at Ni changes dramatically, the bond distances (Ni–Fe, Ni–H, and Fe–H) change by less than 5% (Table 2).

Spin densities were analyzed to determine the localization of the unpaired electron in the mixed-valence reduced bridging hydride species. In these species, the spin resides primarily (41–47%) on the Ni center, although spin density is also localized near the Fe, P, and S centers (Table 6). As observed

Table 6. Spin Densities Calculated for the Reduced Hydride Complex $[H1]^0$

complex	ρ(Ni)	ρ(Fe)	ρ(2S)	$\rho(2P_{Ni})^a$
sym-$[H1]^0$	0.47	0.19	0.14	0.12
unsym-$[H1]^0$	0.41	0.28	0.14	0.12

[a]These values refer to the P atoms of the dppv ligand on the Ni center.

for related NiFe dithiolates,[6,31,32] the spin densities are relatively insensitive to the orientation of the pdt^{2-} ring (Table S16). The spin density plots for both the unsym and sym isomers of $[H1]^0$ are depicted in Figure 10. Overall, the reduction of the bridging hydride species is consistently predicted to occur primarily at the Ni center.

Similar to the parent Ni(II)Fe(II) derivatives, the hydride ligand for the reduced mixed-valence hydrides is also

DOI: 10.1021/jacs.6b04579
J. Am. Chem. Soc. 2016, 138, 9234–9245

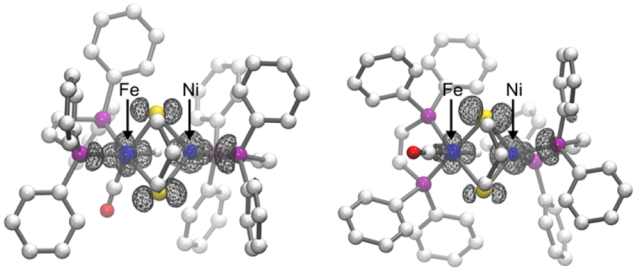

Figure 10. Top-down view of the isocontour plot (isovalue 0.005) of the spin density of $[H\mathbf{1}]^0$ for the unsym (apical basal dppv on Fe, left) and sym (dibasal dppv on Fe, right) isomers showing predominant localization around the Ni coordination sphere, with some localization near Fe as well. This difference is clarified by the numerical atomic spin densities provided in Table 6.

asymmetrically bound, with a shorter distance to Fe than to Ni (Table 2). This asymmetry is consistent with the greater spin density on Ni, which indicates that the species is best described as a Ni(I) paramagnet ligated to an Fe(II) hydride.

Protonation of $[H\mathbf{1}]^0$. The aim of preparing $[H\mathbf{1}]^0$ was to test its role in the hydrogen evolution reaction but in the absence of an electrode. Indeed, when treated with 1 equiv of $HBF_4{\cdot}Et_2O$, solutions of $[H\mathbf{1}]^0$ immediately gave H_2 concomitant with a color change from brown to orange. The $^{31}P\{^1H\}$ NMR spectrum recorded 20 min after the addition of acid showed that a 72:28 mixture of *unsym*-$[H\mathbf{1}]^+$ and *sym*-$[H\mathbf{1}]^+$ is produced in 96% yield. On the basis of the rates of the relevant isomerizations, a ratio of ~75:25 is predicted. Analysis of the headspace by gas chromatography revealed that 0.32 equiv of H_2 is formed. This yield of H_2 corresponds to 64% of the theoretically predicted value according to the stoichiometry in eq 2.

$$[H\mathbf{1}]^0 + H^+ \rightarrow [H\mathbf{1}]^+ + 0.5H_2 \quad (2)$$

In terms of the mechanism for hydrogen evolution, the steps in eqs 3 and 4 are invoked.

protonation of $[H\mathbf{1}]^0$ affords $[\mathbf{1}]^+$ and H_2 (vide infra):

$$[H\mathbf{1}]^0 + H^+ \rightarrow [\mathbf{1}]^+ + H_2 \quad (3)$$

electron transfer from $[H\mathbf{1}]^0$ to $[\mathbf{1}]^+$:

$$[H\mathbf{1}]^0 + [\mathbf{1}]^+ \rightarrow [H\mathbf{1}]^+ + [\mathbf{1}]^0 \quad (4)$$

protonation of $[\mathbf{1}]^0$:

$$[\mathbf{1}]^0 + H^+ \rightarrow [H\mathbf{1}]^+ \quad (5)$$

The redox process in eq 4 is favorable since our electrochemical measurements show that $[H\mathbf{1}]^0$ is about 0.5 V more reducing than $[\mathbf{1}]^0$.

Three predictions arising from the proposed mechanism were tested. First, protonation of $[H\mathbf{1}]^0$ with D^+ sources should give HD. When the reaction of $[H\mathbf{1}]^0$ and DOTf was monitored by ^1H NMR spectroscopy, the HD:H_2 ratio was 5.3:1. Second, treatment of $[H\mathbf{1}]^0$ with a deficiency of H^+ should give some $[\mathbf{1}]^0$. Indeed, addition of 0.5 equiv of $H(OEt_2)_2BAr^F{}_4$ to a solution of $[H\mathbf{1}]^0$ gave substantial but variable amounts of $[\mathbf{1}]^0$. The variability of these yields is attributed to the sensitivity of $[H\mathbf{1}]^0$ toward impurities, which accelerate hydrogen evolution according to eq 1. Finally, the ratio *unsym*-$[H\mathbf{1}]^+$:*sym*-$[H\mathbf{1}]^+$ should reflect on the mechanism since oxidation of $[H\mathbf{1}]^0$ predominantly gives significant sym, and protonation of $[\mathbf{1}]^0$ generates exclusively unsym (see above). Indeed, treatment of an MeCN solution of $[H\mathbf{1}]^0$ with 1 equiv of $HBF_4{\cdot}Et_2O$ led to a 72:28 ratio of *unsym*-$[H\mathbf{1}]^+$ to *sym*-$[H\mathbf{1}]^+$ 20 min after treatment. This ratio is consistent with a mechanism in which half of the $[H\mathbf{1}]^0$ undergoes a sequence

Scheme 5. Experimentally and Computationally Supported Pathway for Hydrogen Evolution Catalyzed by 1[a]

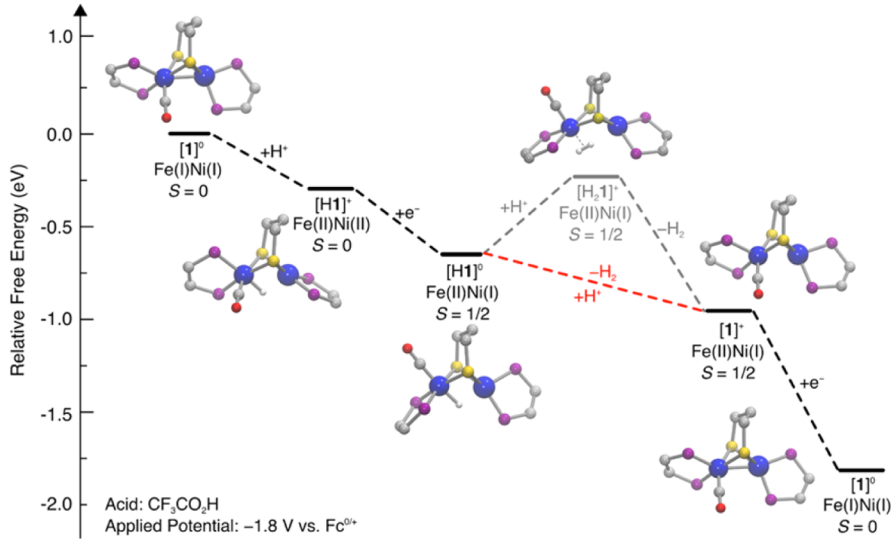

[a]The free energies are calculated with CF_3CO_2H acid (pK_a^{MeCN} = 12.7) and at an applied potential of −1.8 V vs $Fc^{0/+}$ in MeCN to coincide with the bulk electrolysis experiments. H_2 evolution is proposed to occur directly from interaction of $[H\mathbf{1}]^0$ and CF_3CO_2H acid under these conditions (red dashed line), but stronger acids may also evolve H_2 from an intermediate dihydrogen complex, $[H_2\mathbf{1}]^+$ (gray dashed lines). In the last step, an alternative mechanism for reduction of $[\mathbf{1}]^+$ by $[H\mathbf{1}]^0$ could also occur under certain conditions. The relative free energies for half-reactions corresponding to electron transfer are calculated with respect to the applied potential, and the free energy difference between the initial and final states in the pathway corresponds to the potential associated with the double reduction of 2HA to produce $2A^-$ and H_2 relative to this applied potential. An analogous scheme calculated relative to the HA/H_2 couple is presented in Figure S5. Ph−P groups are omitted for clarity.

DOI: 10.1021/jacs.6b04579
J. Am. Chem. Soc. 2016, 138, 9234−9245

Table 7. Comparison of Redox States of Ni−H−Fe Centers in the Enzyme and Models

	$[(RSH)(RS)Ni(\mu\text{-}SR)_2(\mu\text{-}H)Fe(CO)(CN)_2]^{2-}$	$(PR_3)_2Ni(\mu\text{-}SR)_2(\mu\text{-}H)Fe(CO)(PR_3)_2$	$[(RS)_2Ni(\mu\text{-}SR)_2(\mu\text{-}H)Fe(CO)(CN)_2]^{2-}$	$[(PR_3)_2Ni(\mu\text{-}SR)_2(\mu\text{-}H)Fe(CO)(PR_3)_2]^{+}$
label	Ni−R	reduced hydride	Ni−C	oxidized hydride
oxidation states	Ni(II), Fe(II)	Ni(I), Fe(II)	Ni(III), Fe(II)	Ni(II), Fe(II)
net charge	2−	0	2−	1+
reactivity	hydridic	hydridic	protic	protic

of protonation, reduction, and protonation to form almost exclusively *unsym*-$[\mathbf{H1}]^+$, and the other half is oxidized to a mixture of *unsym*-$[\mathbf{H1}]^+$ and *sym*-$[\mathbf{H1}]^+$, which was shown independently to reach a 53:47 ratio 20 min after oxidation in MeCN (vide supra).

Several scenarios for the protonolysis of $[\mathbf{H1}]^0$ were examined with DFT to gain insight into the pathway for H_2 evolution. The free energy diagram for a proposed mechanism is shown in Scheme 5. The free energies were calculated with CF_3CO_2H as the acid (pK_a^{MeCN} = 12.7) and at an applied potential of −1.80 V vs $Fc^{0/+}$ in MeCN, consistent with the bulk electrolysis experiments described above. Under these conditions, DFT calculations indicate that the production of H_2 via interaction of $[\mathbf{H1}]^0$ with CF_3CO_2H acid to give $[\mathbf{1}]^+$ is thermodynamically favorable (ΔG° = −7.0 kcal/mol, indicated by the red dashed line in Scheme 4). This process most likely proceeds by an asynchronous protonation of the hydride and release of H_2. A concerted pathway involving the absence of a thermally stable intermediate is also possible. A pathway involving protonation of the Fe−H bond in $[\mathbf{H1}]^0$ to form an intermediate dihydrogen complex, $[\mathbf{H_2 1}]^+$, is thermodynamically unfavorable (gray dashed lines in Scheme 5) under these specific conditions. This protonation step is more favorable when stronger acids, such as $HBAr^F{}_4{\cdot}2Et_2O$, are used. Under such strong acid conditions, H_2 is evolved directly after the H_2 adduct is formed upon protonation of $[\mathbf{H1}]^0$. Thus, both mechanisms may be involved in H_2 evolution. Regardless, evolution of H_2 produces $[\mathbf{1}]^+$, which is then reduced to form $[\mathbf{1}]^0$ in the bulk electrolysis experiments. However, note that, in the protonation experiments discussed above, an alternative mechanism, in which $[\mathbf{1}]^+$ is reduced by $[\mathbf{H1}]^0$ (eq 4), occurs in the absence of an electrode and could in principle also occur in the electrochemical experiments.

CONCLUSIONS

The pathway has been elucidated for hydrogen evolution catalyzed by a synthetic analogue of the [NiFe]-hydrogenase active site. The model system is $[(dppv)Ni(\mu\text{-}pdt)(\mu\text{-}H)Fe(CO)(dppv)]^+$, which does not release H_2 even upon protonation. Instead, *reduction is required to initiate hydrogen evolution*. Of particular interest is the spectroscopic and computational characterization of the reduced hydride complex, which is stabilized by the steric protection afforded by the two dppv ligands. The reduced hydride complex is assigned as a Ni(I)Fe(II) species on the basis of FT-IR and electron paramagnetic resonance (EPR) measurements and supported by DFT calculations. These studies revealed that reduction of the Ni center enhances the hydridic character of the Fe−H center. Hydrogen evolution occurs by protonation of the Fe−H bond leading to release of dihydrogen. It is intriguing to contrast the hydrogen-evolving properties of $[\mathbf{H1}]^0$ with those of the related mixed-valence homobimetallic complex $[HFe_2(pdt)(CO)_2(dppv)_2]$, where the hydride is a spectator: it is not involved in H_2 release.[14]

Comparisons of these NiFe models with the [NiFe]-hydrogenases are instructive. Overall, the biological system operates at one oxidation state higher than these models (Table 7). This difference reflects the effects of charge, since the model complexes are almost always[7] neutral or cationic, whereas the active site is anionic, which stabilizes higher oxidation states. With seven anionic ligands ($4 \times RS^-$, $2 \times CN^-$, H^-), the active site in the Ni−R state is 3^- or 2^-, depending on the degree of protonation of a terminal thiolate ligand.[9]

Crystallographic and DFT analyses for the Ni−R and Ni−C states in the enzyme reveal that the Ni−H and Fe−H distances are similar, with $d_{Ni-H} \approx 1.6$ and d_{Fe-H} = 1.7 Å.[11] In synthetic models, the Fe−H distances are always shorter than the Ni−H distances, sometimes by 0.6 Å.[4,33] X-ray spectroscopic studies indicate that the Fe−H site only weakly interacts with the Ni center in these models.[33] Studies on both the enzyme and models indicate, however, that these distances are not strongly affected by the metal oxidation state.[9,11] The most prominent difference between the enzyme and the active site models is the coordination sphere of the nickel center.[34] In the models, the $Ni(SR)_2(PR_3)_2$ site alternates between square planar and tetrahedral, whereas, in the protein, the $Ni(SR)_4$ center maintains a distorted SF_4-like geometry.[9,35] Future studies must address these three gaps: the rigidity of the Ni site, the anionic character of the active site, and the fact that redox is confined to Ni. These daunting challenges can best, we believe, be addressed by radical changes in the coordination sphere of the Ni center.

EXPERIMENTAL SECTION

General Considerations. Unless otherwise stated, reactions were conducted using standard Schlenk techniques, reagents were purchased from conventional sources, and solvents were HPLC grade and purified using an alumina filtration system (Glass Contour, Irvine, CA). ESI-MS data were acquired using a Waters Micromass Quattro II or ZMD spectrometer. Analytical data were acquired using an Exeter Analytical CE-440 elemental analyzer. NMR spectra were acquired with Varian U500 and VXR500 spectrometers. Chemical shifts (ppm) were referenced to residual solvent peaks (for ^1H and ^{13}C) or external 85% H_3PO_4 (for ^{31}P). Solution IR spectra were recorded on a PerkinElmer Spectrum 100 FTIR spectrometer. Crystallographic data were collected using a Siemens SMART diffractometer equipped with a Mo Kα source (λ = 0.71073 Å) and an Apex II detector. Photolysis employed a Spectroline MB-100 instrument (365 nm). Syntheses of $Fe(pdt)(CO)_2(dppv)$[36] and $K[FeCp(CO)_2]$[37] have been reported. CVs were simulated with the CHI630D package. EPR spectra were recorded on a Varian E-line E-12 Century series X-band CW spectrometer. Spectra were collected at room temperature with a microwave frequency of 9.30 GHz, 1 G modulation, and 20 mW microwave power. EPR spectra were simulated using the program SIMPOW6.[38] Samples of $[\mathbf{1}]^0$ and $[\mathbf{H1}]^0$ were handled in a glovebox with the exclusion of chlorocarbons.

$[(dppv)Ni(\mu\text{-}Cl)(\mu\text{-}pdt)Fe(CO)(dppv)]BF_4$, $[\mathbf{Cl1}]BF_4$. To a solution of $Fe(pdt)(CO)_2(dppv)$ (1.00 g, 1.63 mmol) in 150 mL of acetone were added solid $NiCl_2(dppv)$ (0.854 g, 1.63 mmol) and $NaBF_4$ (0.196 g, 1.78 mmol). The resulting heterogeneous mixture was heated at reflux for 4 h, at which point no solid was visible, and the

DOI: 10.1021/jacs.6b04579
J. Am. Chem. Soc. 2016, 138, 9234−9245

red color had deepened. An FT-IR spectrum confirmed that $Fe(pdt)(CO)_2(dppv)$ was fully consumed. After being cooled in an ice bath, the reaction solution was filtered through a pad of Celite. The solvent was removed from the filtrate, and the solid was extracted into 50 mL of CH_2Cl_2. The solution was diluted with 150 mL of hexanes, and the mixture was cooled to 0 °C for several days. Crystals of the product were isolated and dried under vacuum. Yield: 1.76 g (93%). ^{1}H NMR (500 MHz, CD_2Cl_2, 20 °C): δ 8.05−7.87 (m, 2H, $P(CH)_2P$), 7.78−7.22 (m, 40H, Ph), 7.14−6.95 (m, 2H, $P(CH)_2P$), 2.05 (s, 1H, $(SCH_2)_2CH_2$), 2.02 (s, 2H, $(SCH_2)_2CH_2$), 2.00−1.93 (m, 2H, $(SCH_2)_2CH_2$), 1.94−1.85 (m, 1H, $(SCH_2)_2CH_2$), 1.04−0.91 (m, 2H, $(SCH_2)_2CH_2$). $^{31}P\{^1H\}$ NMR (202 MHz, CD_2Cl_2): δ 73.3 (d, J_{PP} = 16.6 Hz, 2 P, Fe*P*), 57.6 (d, J_{PP} = 16.5 Hz, 2 P, Ni*P*). IR (acetone): ν_{CO} = 1946 (s) cm^{-1}. Although not obtained in analytical purity ([C] varied by at least 3%), crude samples were converted to the reduced complex.

(dppv)Ni(μ-pdt)Fe(CO)(dppv), [1]^0. In a 500-mL Schlenk flask was dissolved $[Cl\mathbf{1}]BF_4$ (1.25 g, 1.07 mmol) in 200 mL of acetone, and the solution was stirred at room temperature. This solution was treated dropwise with a solution of $K[FeCp(CO)_2]$ (0.464, 2.14 mmol) in 60 mL of distilled acetone. The reaction mixture was allowed to stir for ∼50 min and was then concentrated to ∼100 mL. The solution was diluted with 100 mL of pentane and was cooled in an ice bath for 4 h to yield a brown precipitate. The precipitate was isolated by cannula filtration while cold and rinsed with pentane. The precipitate was then extracted into 2 × 30 mL of cold toluene, and these extracts were filtered through a pad of Celite. The toluene was removed under vacuum, and the remaining brown solid was recrystallized from 50 mL of THF and 150 mL of pentane at −40 °C. Yield: 0.972 g (87%). ^{1}H NMR (500 MHz, C_6D_6): δ 8.08−6.93 (44H, Ph and $P(CH)_2P$), 2.32 (m, 2H, $(SCH_2)CH_2$), 1.79 (m, 1H, $(SCH_2)CH_2$), 1.56 (m, 1H, $(SCH_2)CH_2$); 2H, $(SCH_2)CH_2$). $^{31}P\{^1H\}$ NMR (202 MHz, C_6D_6): δ 89.2 (t, J_{PP} = 13.6 Hz, 2P, Fe2*P*), 74.2 (dt, J_{PP} = 30.1, 15.5 Hz, 1P, Ni*P*), 46.2 (dt, J_{PP} = 28.3, 12.1 Hz, 1P, Ni*P*). IR (THF): ν_{CO} = 1911 (sh), 1897 (s) cm^{-1}. Anal. Calcd for $C_{56}H_{50}FeNiOP_4S_2$: C, 64.58; H, 4.84. Found: C, 64.17; H, 4.70. Single crystals of $[\mathbf{1}]^0$ were grown from THF solutions layered with pentane.

[(dppv)Ni(μ-H)(μ-pdt)Fe(CO)(dppv)]OTf, [H1]OTf. A solution of $[\mathbf{1}]^0$ (0.10 g, 0.10 mmol) in 20 mL of THF was treated with HOTf (10 μL, 0.11 mmol), causing a color change from a brown to an orange solution. The FT-IR spectrum confirmed that the starting material was fully consumed. The solution was concentrated to ∼10 mL. The concentrated solution was layered with 10 mL of pentane and cooled to −40 °C for 4 days. The resulting orange crystals were collected, washed with pentane, and dried under vacuum. Yield: 0.114 g (99%). The following are data for the *sym* isomer. ^{1}H NMR (500 MHz, d_3-MeCN, 20 °C): δ −4.27 (t, $^2J_{PH}$ = 35.3 Hz, 1H, Fe(μ-*H*)Ni). $^{31}P\{^1H\}$ NMR (202 MHz, d_3-MeCN, 20 °C): δ 87.8 (s, 2P, Fe2*P*), 69.1 (s, 2P, *sym*-Ni2*P*). The following are data for the unsym isomer. ^{1}H NMR (500 MHz, d_3-MeCN, 20 °C): δ −5.80 (t, $^2J_{PH}$ = 42.3 Hz, 1H, Fe(μ-*H*)Ni). $^{31}P\{^1H\}$ NMR (202 MHz, d_3-MeCN, 20 °C): δ 93.4 (s, 1P, Fe*P*), 79.4 (s, 1P, Fe*P*), 73.5 (s, 2P, Ni2*P*). IR (THF): ν_{CO} = 1962 (m), 1952 (s) cm^{-1}. Anal. Calcd for $C_{57}H_{51}F_3FeNiO_4P_4S_3$: C, 57.45; H, 4.31. Found: C, 57.22; H, 4.41.

[(dppv)Ni(μ-H)(μ-pdt)Fe(CO)(dppv)]BAr$^F_4$, [H1]BAr$^F_4$. A solution of $[H\mathbf{1}]OTf$ (0.071 g, 0.06 mmol) in 10 mL of THF was treated with $NaBAr^F_4$ (0.058 g, 0.065 mmol), and the reaction mixture was heated to 35 °C for 5 min. After being cooled to room temperature and filtered, the reaction solution was evaporated, leaving an orange solid residue. The following are data for the sym isomer. ^{1}H NMR (500 MHz, C_6D_6, 20 °C): δ −4.37 (t, J_{PH} = 34.0 Hz, 1H, Fe(μ-*H*)Ni). $^{31}P\{^1H\}$ NMR (202 MHz, C_6D_6, 20 °C): δ 88.2 (s, 2P, Fe2*P*), 68.4 (s, 2P, Ni2*P*). The following are data for the unsym isomer. δ 8.45−6.84 (m, 52 H, Ar), 6.42−6.21 (m, 4 H, $P(CH)_2P$, 1.71−1.60 (m, J_{HH} = 11 Hz, 1H, $(SCH_2)CH_2$), 1.49 (d, J_{HH} = 14.1 Hz, 1H, $(SCH_2)CH_2$), 1.45−1.35 (m, 1H, $(SCH_2)CH_2$), 1.03−0.95 (m, 2H, $(SCH_2)CH_2$), 0.10 (t, J_{HH} = 13.5 Hz, 1H, $(SCH_2)CH_2$), −5.77 (t, $^2J_{PH}$ = 42.5 Hz, 1H, Fe(μ-*H*)Ni). $^{31}P\{^1H\}$ NMR (202 MHz, C_6D_6, 20 °C): δ 87.82 (s, 1P, Fe*P*), 80.60 (s, 1P, Fe*P*), 72.82 (s, 2P, Ni2*P*). IR (THF): ν_{CO} = 1953 (s), 1960 (sh).

[(dppv)Ni(μ-H)(μ-pdt)Fe(CO)(dppv)]BF$_4$, [H1]BF$_4$. A solution of $[\mathbf{1}]^0$ (0.500 g, 0.48 mmol) in 75 mL of THF was treated with HBF_4·Et_2O (0.1 M, 0.5 mL, 0.05 mmol) to give an orange solution. After being concentrated to half-volume, the solution was layered with 100 mL of pentane at 0 °C. Small orange crystals were collected by filtration and dried under vacuum. Yield: 0.485 g (90%). The unsymmetrical isomer crystallized exclusively. ^{1}H NMR (500 MHz, CD_2Cl_2, 20 °C): δ 8.10 (t, $^2J_{PH}$ = 8.3 Hz, 2H, $P(CH)_2P$)), 7.71−7.12 (m, 40H, Ph), 6.91−6.77 (m, 2H, $P(CH)_2P$), 1.54 (t, J_{HH} = 14.4 Hz, 1H, $(SCH_2)CH_2$), 1.36−1.23 (m, 1H, $(SCH_2)CH_2$), 1.09 (d, J_{HH} = 15.8 Hz, 1H, $(SCH_2)CH_2$), 0.96 (d, J_{HH} = 12.7 Hz, 1H, $(SCH_2)CH_2$), 0.89 (d, J_{HH} = 7.3 Hz, 1H, $(SCH_2)CH_2$), 0.09 (d, J_{HH} = 12.8 Hz, 1H, $(SCH_2)CH_2$), −5.79 (t, $^2J_{PH}$ = 42.3 Hz, 1H, Fe(μ-*H*)Ni). $^{31}P\{^1H\}$ NMR (202 MHz, CD_2Cl_2, 20 °C): δ 87.82 (s, 1P, Fe*P*), 80.60 (s, 1P, Fe*P*), 72.82 (s, 2P, Ni2*P*). IR (THF): ν_{CO} = 1963 (sh), 1951 (s) cm^{-1}. Anal. Calcd for $C_{56}H_{51}BF_4FeNiOP_4S_2$: C, 59.56; H, 4.55. Found: C, 58.62; H, 4.66.

[(dppv)Ni(μ-H)(μ-pdt)Fe(CO)(dppv)], [H1]^0. To a suspension of $[H\mathbf{1}]BF_4$ (0.100 g, 0.09 mmol) in Et_2O (500 μL) was added a solution of Cp^*_2Co (0.029 g, 0.09 mmol) in Et_2O (500 μL). After 5 min, the darkened solution was filtered through a pad of Celite, which was rinsed with Et_2O (∼2 mL). Solvents were removed under vacuum, leaving a dark brown, almost black solid. Yield: 0.075 g (81%). IR (THF): ν_{CO} = 1920 cm^{-1}. Anal. Calcd for $C_{56}H_{51}FeNiOP_4S_2$: C, 64.51; H, 4.93. Found: C, 64.47; H, 5.28. Samples were handled in a glovebox with the exclusion of chlorocarbons.

Computational Methods. The DFT calculations were performed with the BP86 functional[39] with the SDD pseudopotential and associated basis set[40] for Ni and Fe, the 6-31G** basis set[41] for the μ-H ligands, and the 6-31G* basis set[42] for all other atoms. The starting coordinates for the geometry optimizations of $[\mathbf{1}]^0$ and $[H\mathbf{1}]^+$ were obtained from the available crystal structures, and starting coordinates for species without crystal structures were obtained by manually altering closely related crystal structures prior to optimizations. The conductor-like polarizable continuum model[43] was used to calculate the solvation free energies using the Bondi atomic radii[44] and including nonelectrostatic contributions from dispersion,[45] repulsion,[45] and cavitation formation.[46] The solvent was acetonitrile (MeCN) unless stated otherwise. Structural and energetic information for all studied compounds are provided in the Supporting Information (Tables S19−S54).

Herein, the geometry optimizations were performed in the gas phase; however, a comparison of the structures optimized in the gas and solution phases is provided in the Supporting Information (Tables S9−S12). All minimum energy structures were verified to have no imaginary frequencies, and all transition states (TSs) were confirmed to have only a single imaginary frequency. The TSs were located utilizing the synchronous transit-guided quasi-Newton method,[47] and the intrinsic reaction coordinate (IRC) was followed using the local quadratic approximation[48] to verify that the TS leads to the correct reactant and product states. Thermochemical data were calculated at T = 298.15 K. The zero-point energy, entropic contributions, and solvation effects were included in the calculated reaction free energies (ΔG) and free energy barriers ($\Delta G^{\ddagger}$) in solution. The relative reduction potentials and pK_a values were calculated using methodology described elsewhere.[49] Pipek−Mezey localization was performed using keyword IOp(4/9=20212). All calculations were performed with the Gaussian 09 electronic structure program.[50]

■ ASSOCIATED CONTENT

Supporting Information

The Supporting Information is available free of charge on the ACS Publications website at DOI: 10.1021/jacs.6b04579.

Experimental and computational data (PDF)

■ AUTHOR INFORMATION

Corresponding Authors

*shs3@illinois.edu

DOI: 10.1021/jacs.6b04579
J. Am. Chem. Soc. 2016, 138, 9234−9245

*rauchfuz@illinois.edu

Author Contributions

†O.A.U., M.T.H., and C.P.R. contributed equally to this work.

Notes

The authors declare no competing financial interest.

■ ACKNOWLEDGMENTS

The research reported in this paper was supported by the National Institute of General Medical Sciences of the National Institutes of Health under Award Number GM061153. The computational portion of this work was funded by the National Science Foundation Graduate Research Fellowship Program under Grant Number DGE-1144245 (M.T.H.) and by the National Science Foundation under Grant CHE-13-61293. We thank Drs. Noémie Lalaoui and David Schilter for helpful advice.

■ REFERENCES

(1) Lansing, J. C.; Manor, B. C.; Rauchfuss, T. B. In *Encyclopedia of Inorganic and Bioinorganic Chemistry*; Scott, R. A., Ed.; John Wiley: Chichester, U.K., 2014; pp 1−21.
(2) Barton, B. E.; Whaley, C. M.; Rauchfuss, T. B.; Gray, D. L. *J. Am. Chem. Soc.* **2009**, *131*, 6942−6943.
(3) Barton, B. E.; Rauchfuss, T. B. *J. Am. Chem. Soc.* **2010**, *132*, 14877−14885.
(4) Ogo, S.; Ichikawa, K.; Kishima, T.; Matsumoto, T.; Nakai, H.; Kusaka, K.; Ohhara, T. *Science* **2013**, *339*, 682−684.
(5) Carroll, M. E.; Barton, B. E.; Gray, D. L.; Mack, A. E.; Rauchfuss, T. B. *Inorg. Chem.* **2011**, *50*, 9554−9563.
(6) Huynh, M. T.; Schilter, D.; Hammes-Schiffer, S.; Rauchfuss, T. B. *J. Am. Chem. Soc.* **2014**, *136*, 12385−12395.
(7) Manor, B. C.; Rauchfuss, T. B. *J. Am. Chem. Soc.* **2013**, *135*, 11895−11900.
(8) Bullock, R. M.; Appel, A. M.; Helm, M. L. *Chem. Commun.* **2014**, *50*, 3125−3143. Yang, J. Y.; Bullock, R. M.; Rakowski DuBois, M.; DuBois, D. L. *MRS Bull.* **2011**, *36*, 39−47. *Bioinspired Catalysis*; Schollhammer, P., Weigand, W., Eds.; Wiley-VCH: Weinheim, Germany, 2015.
(9) Lubitz, W.; Ogata, H.; Rüdiger, O.; Reijerse, E. *Chem. Rev.* **2014**, *114*, 4081−4148.
(10) Siegbahn, P. E. M.; Tye, J. W.; Hall, M. B. *Chem. Rev.* **2007**, *107*, 4414−4435.
(11) Ogata, H.; Nishikawa, K.; Lubitz, W. *Nature* **2015**, *520*, 571−574.
(12) Greene, B. L.; Wu, C.-H.; McTernan, P. M.; Adams, M. W. W.; Dyer, R. B. *J. Am. Chem. Soc.* **2015**, *137*, 4558−4566. Hidalgo, R.; Ash, P. A.; Healy, A. J.; Vincent, K. A. *Angew. Chem., Int. Ed.* **2015**, *54*, 7110−7113.
(13) Canaguier, S.; Field, M.; Oudart, Y.; Pécaut, J.; Fontecave, M.; Artero, V. *Chem. Commun.* **2010**, *46*, 5876−5878.
(14) Wang, W.; Nilges, M. J.; Rauchfuss, T. B.; Stein, M. *J. Am. Chem. Soc.* **2013**, *135*, 3633−3639.
(15) Carroll, M. E.; Barton, B. E.; Rauchfuss, T. B.; Carroll, P. J. *J. Am. Chem. Soc.* **2012**, *134*, 18843−18852.
(16) Jablonskytė, A.; Wright, J. A.; Fairhurst, S. A.; Peck, J. N. T.; Ibrahim, S. K.; Oganesyan, V. S.; Pickett, C. J. *J. Am. Chem. Soc.* **2011**, *133*, 18606−18609.
(17) Schilter, D.; Camara, J. M.; Huynh, M. T.; Hammes-Schiffer, S.; Rauchfuss, T. B. *Chem. Rev.* **2016**, DOI: 10.1021/acs.chemrev.6b00180. Rauchfuss, T. B. *Acc. Chem. Res.* **2015**, *48*, 2107−2116.
(18) Gao, W.; Ekström, J.; Liu, J.; Chen, C.; Eriksson, L.; Weng, L.; Åkermark, B.; Sun, L. *Inorg. Chem.* **2007**, *46*, 1981−1991. Ezzaher, S.; Capon, J.-F.; Gloaguen, F.; Pétillon, F. Y.; Schollhammer, P.; Talarmin, J. *Inorg. Chem.* **2007**, *46*, 9863−9872.
(19) Zhu, W.; Marr, A. C.; Wang, Q.; Neese, F.; Spencer, D. J. E.; Blake, A. J.; Cooke, P. A.; Wilson, C.; Schröder, M. *Proc. Natl. Acad. Sci. U. S. A.* **2005**, *102*, 18280−18285.
(20) Chatt, J.; Kan, C. T.; Leigh, G. J.; Pickett, C. J.; Stanley, D. R. *J. Chem. Soc., Dalton Trans.* **1980**, 2032−2038. Lever, A. B. P. *Inorg. Chem.* **1990**, *29*, 1271−1285.
(21) Glendening, E. D.; Reed, A. E.; Carpenter, J. E.; Weinhold, F. *NBO*, version 3.1; University of Wisconsin System: Madison, WI, 1996.
(22) Pipek, J.; Mezey, P. G. *J. Chem. Phys.* **1989**, *90*, 4916−4926.
(23) Justice, A. K. Ph.D. Thesis, University of Illinois at Urbana-Champaign, 2008.
(24) Chambers, G. M.; Huynh, M. T.; Li, Y.; Hammes-Schiffer, S.; Rauchfuss, T. B.; Reijerse, E.; Lubitz, W. *Inorg. Chem.* **2016**, *55*, 419−431.
(25) Kramarz, K. W.; Norton, J. R. *Prog. Inorg. Chem.* **1994**, *42*, 1−65.
(26) Kozak, A.; Czaja, M.; Chmurzynski, L. *J. Chem. Thermodyn.* **2006**, *38*, 599.
(27) Berning, D. E.; Noll, B. C.; DuBois, D. L. *J. Am. Chem. Soc.* **1999**, *121*, 11432−11447.
(28) Apfel, U.-P.; Troegel, D.; Halpin, Y.; Tschierlei, S.; Uhlemann, U.; Görls, H.; Schmitt, M.; Popp, J.; Dunne, P.; Venkatesan, M.; Coey, M.; Rudolph, M.; Vos, J. G.; Tacke, R.; Weigand, W. *Inorg. Chem.* **2010**, *49*, 10117−10132. Greco, C.; Zampella, G.; Bertini, L.; Bruschi, M.; Fantucci, P.; De Gioia, L. *Inorg. Chem.* **2007**, *46*, 108−116. Felton, G. A. N.; Vannucci, A. K.; Chen, J.; Lockett, L. T.; Okumura, N.; Petro, B. J.; Zakai, U. I.; Evans, D. H.; Glass, R. S.; Lichtenberger, D. L. *J. Am. Chem. Soc.* **2007**, *129*, 12521−12530.
(29) Fourmond, V.; Jacques, P.-A.; Fontecave, M.; Artero, V. *Inorg. Chem.* **2010**, *49*, 10338−10347.
(30) Gloaguen, F. *Inorg. Chem.* **2016**, *55*, 390−398.
(31) Schilter, D.; Nilges, M. J.; Chakrabarti, M.; Lindahl, P. A.; Rauchfuss, T. B.; Stein, M. *Inorg. Chem.* **2012**, *51*, 2338−2348.
(32) Schilter, D.; Rauchfuss, T. B.; Stein, M. *Inorg. Chem.* **2012**, *51*, 8931−8941.
(33) Hugenbruch, S.; Shafaat, H. S.; Kramer, T.; Delgado-Jaime, M. U.; Weber, K.; Neese, F.; Lubitz, W.; DeBeer, S. *Phys. Chem. Chem. Phys.* **2016**, *18*, 10688−10699.
(34) Tard, C.; Pickett, C. J. *Chem. Rev.* **2009**, *109*, 2245−2274.
(35) Keith, J. M.; Hall, M. B. *Inorg. Chem.* **2010**, *49*, 6378−6380.
(36) Carroll, M. E.; Chen, J.; Gray, D. E.; Lansing, J. C.; Rauchfuss, T. B.; Schilter, D.; Volkers, P. I.; Wilson, S. R. *Organometallics* **2014**, *33*, 858−867.
(37) Ellis, J. E.; Flom, E. A. *J. Organomet. Chem.* **1975**, *99*, 263−268.
(38) Nilges, M. J.; Matteson, K.; Belford, R. L. In *ESR Spectroscopy in Membrane Biophysics*; Hemminga, M. A., Berliner, L., Eds.; Biological Magnetic Resonance, Vol. *27*; Springer: New York, 2007.
(39) Perdew, J. P. *Phys. Rev. B: Condens. Matter Mater. Phys.* **1986**, *B34*, 7406. Becke, A. D. *Phys. Rev. A: At., Mol., Opt. Phys.* **1988**, *38*, 3098−3100.
(40) Dolg, M.; Wedig, U.; Stoll, H.; Preuss, H. *J. Chem. Phys.* **1987**, *86*, 866−872.
(41) Hariharan, P. C.; Pople, J. A. *Theoret. Chim. Acta* **1973**, *28*, 213−222.
(42) Hehre, W. J.; Ditchfield, R.; Pople, J. A. *J. Chem. Phys.* **1972**, *56*, 2257−2261. Francl, M. M.; Pietro, W. J.; Hehre, W. J.; Binkley, J. S.; Gordon, M. S.; DeFrees, D. J.; Pople, J. A. *J. Chem. Phys.* **1982**, *77*, 3654−3665.
(43) Barone, V.; Cossi, M. *J. Phys. Chem. A* **1998**, *102*, 1995−2001. Cossi, M.; Rega, N.; Scalmani, G.; Barone, V. *J. Comput. Chem.* **2003**, *24*, 669−681.
(44) Bondi, A. *J. Phys. Chem.* **1964**, *68*, 441−451.
(45) Floris, F.; Tomasi, J. *J. Comput. Chem.* **1989**, *10*, 616−627. Floris, F. M.; Tomasi, J.; Ahuir, J. L. P. *J. Comput. Chem.* **1991**, *12*, 784−791.
(46) Pierotti, R. A. *Chem. Rev.* **1976**, *76*, 717−726.
(47) Peng, C.; Bernhard Schlegel, H. *Isr. J. Chem.* **1993**, *33*, 449−454. Peng, C.; Ayala, P. Y.; Schlegel, H. B.; Frisch, M. J. *J. Comput. Chem.* **1996**, *17*, 49−56.
(48) Page, M.; McIver, J. W. *J. Chem. Phys.* **1988**, *88*, 922−935. Koseki, S.; Gordon, M. S. *J. Phys. Chem.* **1989**, *93*, 118−125.

DOI: 10.1021/jacs.6b04579
J. Am. Chem. Soc. 2016, 138, 9234−9245

(49) Qi, X.-J.; Fu, Y.; Liu, L.; Guo, Q.-X. *Organometallics* **2007**, *26*, 4197−4203. Solis, B. H.; Hammes-Schiffer, S. *Inorg. Chem.* **2011**, *50*, 11252−11262. Fernandez, L. E.; Horvath, S.; Hammes-Schiffer, S. *J. Phys. Chem. C* **2012**, *116*, 3171−3180. Solis, B. H.; Hammes-Schiffer, S. *Inorg. Chem.* **2014**, *53*, 6427−6443.

(50) Frisch, M. J.; Trucks, G. W.; Schlegel, H. B.; Scuseria, G. E.; Robb, M. A.; Cheeseman, J. R.; Scalmani, G.; Barone, V.; Mennucci, B.; Petersson, G. A.; Nakatsuji, H.; Caricato, M.; Li, X.; Hratchian, H. P.; Izmaylov, A. F.; Bloino, J.; Zheng, G.; Sonnenberg, J. L.; Hada, M.; Ehara, M.; Toyota, K.; Fukuda, R.; Hasegawa, J.; Ishida, M.; Nakajima, T.; Honda, Y.; Kitao, O.; Nakai, H.; Vreven, T.; Montgomery, J. A.; Peralta, J. E.; Ogliaro, F.; Bearpark, M.; Heyd, J. J.; Brothers, E.; Kudin, K. N.; Staroverov, V. N.; Kobayashi, R.; Normand, J.; Raghavachari, K.; Rendell, A.; Burant, J. C.; Iyengar, S. S.; Tomasi, J.; Cossi, M.; Rega, N.; Millam, J. M.; Klene, M.; Knox, J. E.; Cross, J. B.; Bakken, V.; Adamo, C.; Jaramillo, J.; Gomperts, R.; Stratmann, R. E.; Yazyev, O.; Austin, A. J.; Cammi, R.; Pomelli, C.; Ochterski, J. W.; Martin, R. L.; Morokuma, K.; Zakrzewski, V. G.; Voth, G. A.; Salvador, P.; Dannenberg, J. J.; Dapprich, S.; Daniels, A. D.; Farkas; Foresman, J. B.; Ortiz, J. V.; Cioslowski, J.; Fox, D. J. *Gaussian 09*, revision D.01; Gaussian, Inc.: Wallingford, CT, 2010.

DOI: 10.1021/jacs.6b04579
J. Am. Chem. Soc. 2016, 138, 9234−9245